JACS
JOURNAL OF THE AMERICAN CHEMICAL SOCIETY
Article
pubs.acs.org/JACS

The New Phase $[Tl_4Sb_6Se_{10}][Sn_5Sb_2Se_{14}]$: A Naturally Formed Semiconducting Heterostructure with Two-Dimensional Conductance

Lei Fang,[†] Ratnasabapathy G. Iyer,[†,‡] Gangjian Tan,[†] Damien J. West,[§] Shengbai Zhang,[§] and Mercouri G. Kanatzidis*[,†,∥]

[†]Department of Chemistry, Northwestern University, Evanston, Illinois 60208, United States
[‡]Department of Chemistry, Claflin University, Orangeburg, South Carolina 29118, United States
[§]Department of Physics, Applied Physics, and Astronomy, Rensselaer Polytechnic Institute, Troy, New York 12180-3590, United States
[∥]Materials Science Division, Argonne National Laboratory, Argonne, Illinois 60439, United States

Supporting Information

ABSTRACT: We report on a new layered semiconductor $Tl_8Sn_{10}Sb_{16}Se_{48}$ with an indirect band gap of 0.45 eV. The novel structure is made of alternating layers of $SnSe_2$-type $[Sn_5Sb_2Se_{14}]$ and SnSe-type $[Tl_4Sb_6Se_{10}]$. The material exhibits two-dimensional (2D) electron variable range hopping at low temperatures, indicating an absence of interlayer coherency of the electronic state. Theoretical calculations unveil a 2D confinement for electrons in the $[Sn_5Sb_2Se_{14}]$ sheet and confirm the heterostructure nature. This unique electronic structure is attributed to the weak interlayer coupling and structure distortion in the electron-poor $[Tl_4Sb_6Se_{10}]$ layer that energetically impedes electron propagation.

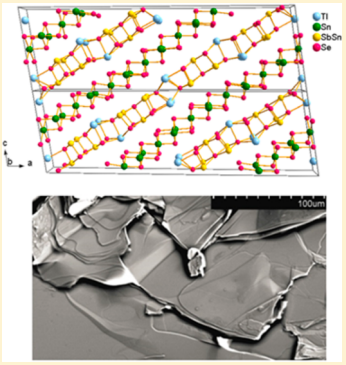

INTRODUCTION

The class of layered semiconductors is increasingly the focus of investigation due to unique electronic properties, novel physics, and the promise of impacting next generation microelectronic devices.[1−3] Few-layer graphite and its monolayer graphene have ignited great enthusiasm to pursue high performing transistors.[4] Monolayer MoS_2, due to the dominance of quantum confinement at atomic scale, exhibits novel properties of indirect-to-direct bandgap transitions and potentials for optoelectronics application.[5−8] Layered semiconductors also raise numerous opportunities for energy harvesting and conversion, for instance, the ultralow thermal conductivity of WSe_2, $(PbSe)_m(TiSe_2)_n$, and SnSe have prompted expectations for high performing thermoelectric device fabrication.[9−11] In the $(PbSe)_m(TiSe_2)_n$ structural motif, the two types of slabs are neutral. One however can derive similar structures using a charge balancing syllogism where one slab is positive and one negative. This can be accomplished by introducing trivalent atoms in the PbSe-type slab and trivalent atoms in the $TiSe_2$-type slab, respectively. This line of thinking led to the new material described here. In this communication, we report on the discovery of the semiconductor $Tl_8Sn_{10}Sb_{16}Se_{48}$, which consists of alternatively grown layers of $[Sn_5Sb_2Se_{14}]$ and $[Tl_4Sb_6Se_{10}]$. Strong lattice distortion happens in the layer $[Tl_4Sb_6Se_{10}]$. Electrical transport measurements exhibit a predominant low-dimensional characteristic that is the 2D electron variable range hopping. First-principles calculations show a heterostructure-like electronic state of $Tl_8Sn_{10}Sb_{16}Se_{48}$, a conductive layer of $[Sn_5Sb_2Se_{14}]$ and a near-insulating layer $[Tl_4Sb_6Se_{10}]$. Low thermal conductivity, $\kappa \approx 0.4$ W/mK, was observed in polycrystalline samples at room temperature. This low thermal conductivity is related to the distorted lattice of $[Tl_4Sb_6Se_{10}]$.

RESULTS AND DISCUSSION

The layered structure of $Tl_8Sn_{10}Sb_{16}Se_{48}$ is shown in Figure 1a. Details of the crystallographic information and structure refinement are provided in Table 1. The compound can be formulated as $(Tl^+)_8(Sn^{4+})_{10}(Sb^{3+})_{16}(Se^{2-})_{48}$. The first building block, $[Sn_5Sb_2Se_{14}]$, adopts the $SnSe_2$-type structure, in which Sn and Sb ions sit in the center of Se octahedra. The Sn and Sb atoms are virtually indistinguishable by X-ray diffraction. With this understanding and for convenience here, we assign one M center as Sb, and the rest as Sn. Details are described in Supporting Information. The second block $[Tl_4Sb_6Se_{10}]$ is a SnSe-type slab. The presence of Tl in this block generates an atomic-level displacement likely due to its lone pair and creates

Received: May 27, 2014
Published: July 24, 2014

   dx.doi.org/10.1021/ja505301y | J. Am. Chem. Soc. 2014, 136, 11079−11084

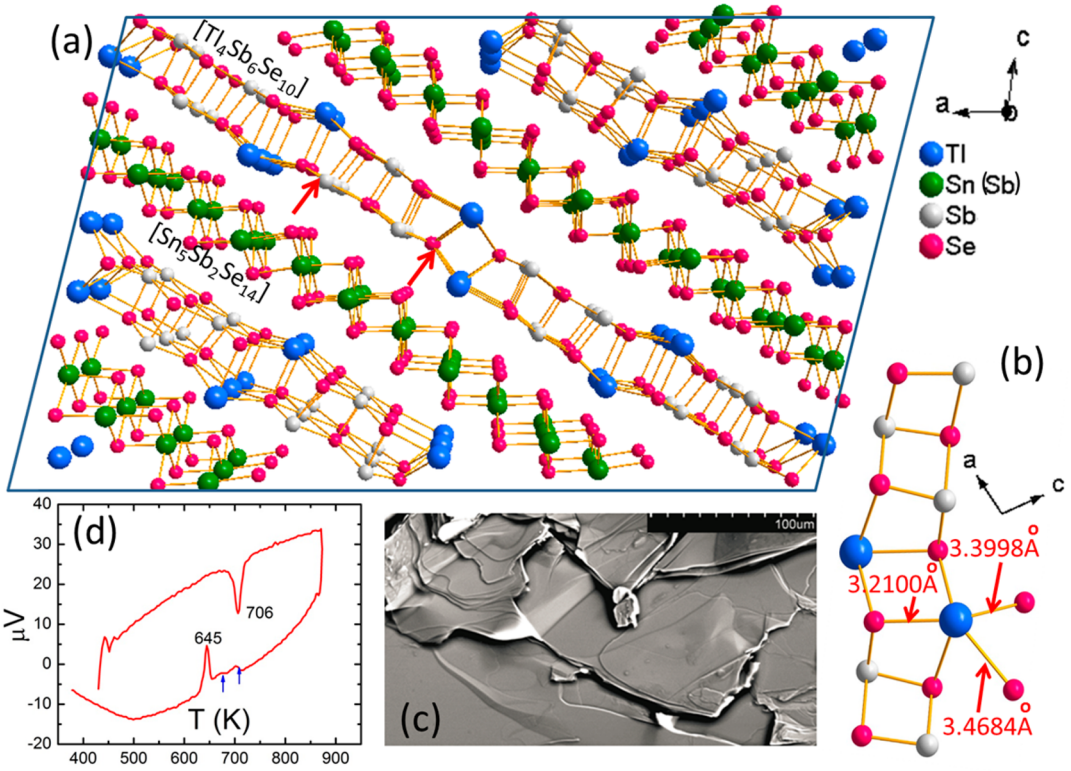

Figure 1. (a) Crystal structure of $Tl_8Sn_{10}Sb_{16}Se_{48}$. The $[Tl_4Sb_6Se_{10}]$ layer is distorted from perfect planarity, while the $[Sn_5Sb_2Se_{14}]$ slab is flat. (b) The interlayer Tl−Se bonds length ranges from 3.4684 to3.3998 Å. (c) SEM image of a fragment of $Tl_8Sn_{10}Sb_{16}Se_{48}$ crystal. EDS shows a composition "$Tl_8Sn_{11.23}Sb_{17.22}Se_{56.13}$", which approximately agrees with the real composition. (d) Differential thermal analysis of $Tl_8Sn_{10}Sb_{16}Se_{48}$ showing a melting point of 706 K and a recrystallization point of 645 K. The arrowed peaks come from minor impurities.

Table 1. Crystal Data and Structure Refinement Details for $Tl_8Sn_{10}Sb_{16}Se_{48}$ at 293 K

empirical formula	$Tl_8Sn_{10}Sb_{16}Se_{48}$
formula wt	8560.40
	293(2) K
wavelength	0.71073 Å
space group	*C*2/*m*
unit cell dimensions	a = 42.950(3) Å, α = 90.00°
	b = 3.967(2) Å, β = 98.813(11)°
	c = 13.369(8) Å, γ = 90.00°
volume	2251(2) Å^3
Z	6
density (calculated)	6.297 g/cm^3
absorp coeff	40.921 mm^{-1}
F(000)	3588
θ range for data collection	1.54−28.21°
index ranges	$-40 \le h \le 56$, $-2 \le k \le 5$, $-17 \le l \le 16$
reflns collected	5347
indep reflns	2768 [R_{int} = 0.0558]
refinement method	Full-matrix least-squares on F^2
data/restraints/params	2768/0/125
GOF	0.954
final R indices[a] [$>2\sigma(I)$]	R_{obs} = 0.0572, wR_{obs} = 0.1290
R indices[a] [all data]	R_{all} = 0.1179, wR_{all} = 0.1551
largest diff. peak and hole	3.608 and −2.871 e·Å^{-3}

[a] $R = \sum||F_o| - |F_c||/\sum|F_o|$; $wR_2 = \{\sum[w(|F_o|^2 - |F_c|^2)^2]/\sum[w(|F_o|^4)]\}^{1/2}$; $w = 1/[\sigma^2(F_o^2) + (0.0809P)^2 + 0.0000P]$, where $P = (F_o^2 + 2F_c^2)/3$.

slight protrusions out of the SnSe-type layer. The lone pairs around the Sb^{3+} atoms (valence electrons $4d^{10}5s^2$) cause the strong distortions in the $[Tl_4Sb_6Se_{10}]$. The presence of Sn^{4+} in these positions is limited because Sn^{4+} (valence electrons $4d^{10}$) favors an isotropic bonding environment (tetrahedral or octahedral).

The $[Sn_5Sb_2Se_{14}]^{2-}$ is a three-atom-thick slab, whereas the $[Tl_4Sb_6Se_{10}]^{2+}$ is two-atom-thick. The two building blocks are charge balanced and alternatively stack along the [101] direction forming the so-called heterostructure. The interlayer coupling is sustained by long Tl−Se bonds ranging from 3.4684 to 3.3998 Å. These bonds and the intralayer Tl−Se bonds are illustrated in Figure 1b. The intraslab bond lengths are shorter at 3.3334−3.2100 Å. Bonding strength decays significantly for lengths longer than 3 Å,[12] and the interlayer coupling in $Tl_8Sn_{10}Sb_{16}Se_{48}$ is therefore weak, endowing the material with pronounced 2D characteristics. Another primary structural feature is the distortion in $[Tl_4Sb_6Se_{10}]$. As marked by arrows in Figure 1a, the displacement induced by the Tl ions buckles the SnSe-type layer by a period of 10 Å. These distortions introduce an additional periodic scattering potential to both the in-plane charge carriers and phonon excitations. In contrast to the distorted $[Tl_4Sb_6Se_{10}]$ layer, the $[Sn_5Sb_2Se_{14}]$ slab is flat. The structural disparity of the two building blocks, together with the weak interlayer coupling, produce a unique 2D electronic structure in $Tl_8Sn_{10}Sb_{16}Se_{48}$, which is attested by our comprehensive transport measurements and theoretical calculations presented below.

In-plane measurements were conducted on single crystal samples from 300 to 2 K. Figure 2a shows that the resistivity at 300 K is ∼0.1 Ω cm and increases with decreasing temperature. This thermally activated behavior arises from the thermal excitation of charge carriers from in-gap impurity states to the

dx.doi.org/10.1021/ja505301y | J. Am. Chem. Soc. 2014, 136, 11079−11084

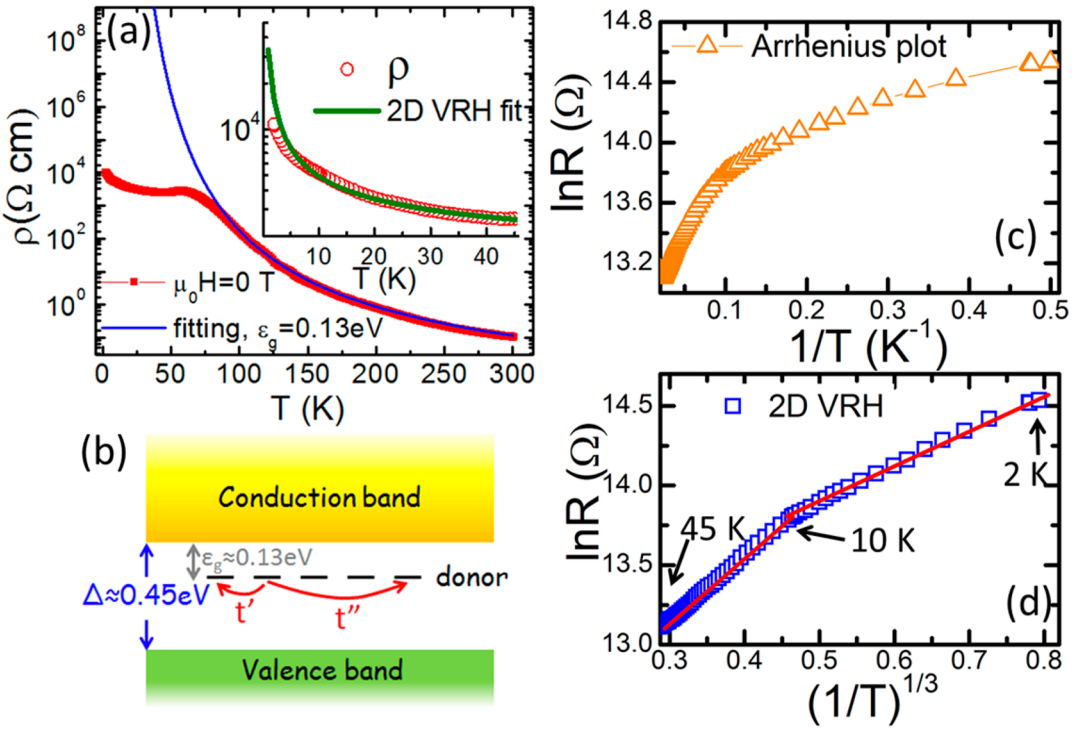

Figure 2. (a) Temperature dependence of the in-plane resistivity of a single crystal sample of $Tl_8Sn_{10}Sb_{16}Se_{48}$. The solid blue curve is a fit including the effects of thermal excitation and impurity scattering. The inset is the low temperature resistivity, and it is fitted using the equation of 2D electron variable range hopping. (b) Schematic showing the band environment of the *n*-doped $Tl_8Sn_{10}Sb_{16}Se_{48}$. *t′* and *t″* denote electron hopping with different hopping distances. (c) The Arrhenius plot of the resistance with respect to inverse temperature. (d) ln *R* is linearly proportional to $(1/T)^{1/3}$, indicating the 2D characteristic of electron hopping.

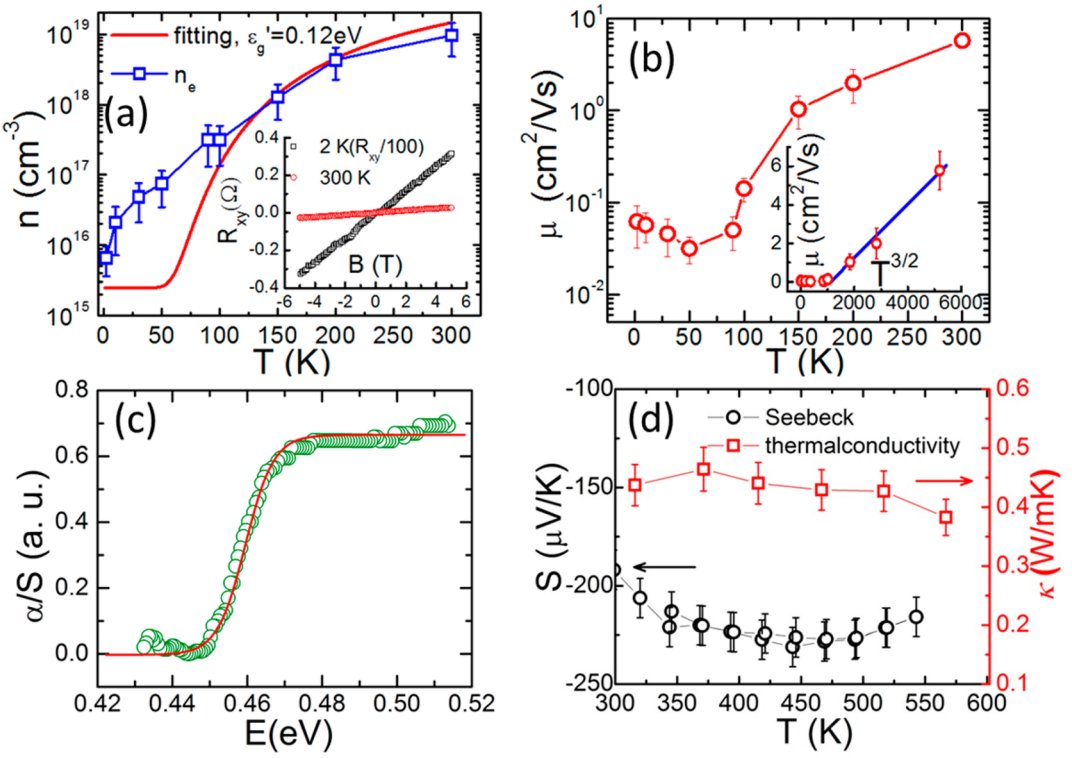

Figure 3. (a) Temperature dependence of the carrier concentration. The red curve is a simulation of temperature dependent ionized carrier concentration and the low temperature freeze-out regime. The inset is the field dependence of the transverse resistance, R_{xy}, at different temperatures. (b) Temperature dependent mobility. The inset is a plot of mobility with respect to $T^{3/2}$. (c) Electronic absorption spectrum of $Tl_8Sn_{10}Sb_{16}Se_{48}$ indicating a band gap of ~0.45 eV. The solid lines in panels b and c are guides to the eye. The "*S*" in the unit of vertical axis denotes scattering coefficient. (d) Temperature dependent Seebeck coefficient and thermal conductivity of a polycrystalline sample of $Tl_8Sn_{10}Sb_{16}Se_{48}$.

dx.doi.org/10.1021/ja505301y | J. Am. Chem. Soc. 2014, 136, 11079−11084

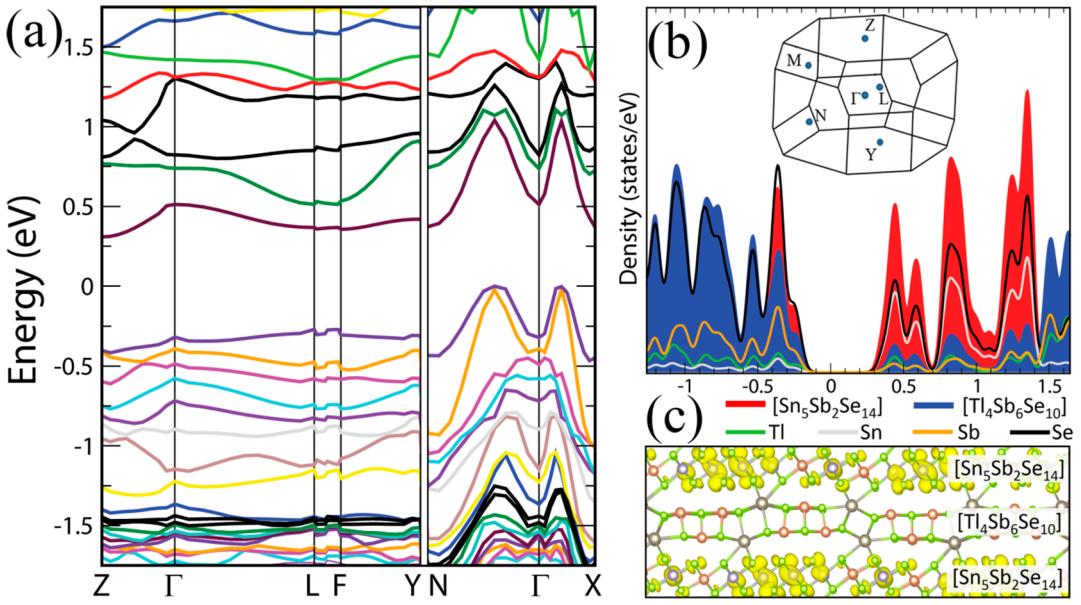

Figure 4. (a) Band dispersion calculated by the hybrid functional method. The calculation shows a direct gap of 0.6 eV between L and F and an indirect gap of 0.3 eV from Z to between Γ and N (~0.4N). (b) Density of states of the valence bands and conduction bands. The inset is a scheme of the Brillouin zone of $Tl_8Sn_{10}Sb_{16}Se_{48}$. (c) The isosurface of the conduction electron density mapped on the crystal structure. It indicates a confinement of the majority electrons in the $[Sn_5Sb_2Se_{14}]$ layer. The intervening $[Tl_4Sb_6Se_{10}]$ layer is not favorable for electron propagation.

conduction band. With the classic thermal excitation model,[13] an energy level of an in-gap impurity state is located ~0.13 eV below the conduction band minimum (CBM). For details of the impurity state, see Supporting Information. At lower temperatures T < 100 K, $\rho(T)$ starts to saturate at decreasing temperatures and exhibits a mild upturn below 50 K, indicating the appearance of another charge transport mechanism. This phenomenon could relate to the thermal excitations of shallow-level donors. However, as shown in Figure 2c, the Arrhenius plot of thermal excitation for temperatures below 50 K exhibits a nonlinear dependence between ln ρ and $1/T$, ruling out a conventional thermal excitation mechanism. This anomalous temperature dependence can be better described by electron hopping between in-gap impurity states. In doped semiconductors, intense impurity scattering localizes electrons.[14] Instead of diffusion, electrons transport via hopping between localized states. This transport mechanism is referred to as electron variable range hopping (VRH).[15] VRH generally happens in disordered semiconductors,[16] nanostructures,[17] DNA,[18] etc. The temperature dependence of resistivity in the VRH regime is written as

$$\ln\left(\frac{\rho(T)}{\rho_0}\right) = \left(\frac{T_0}{T}\right)^{\alpha} \quad (1)$$

where ρ_0 is a temperature independent constant and T_0 is the characteristic temperature. The exponent α equals 1/2, 1/3, and 1/4 for 1D, 2D, and 3D systems, respectively, although, α = 1/2 also satisfies the Coulomb interaction between electrons.[19] As shown in Figure 2d, ln $\rho(T)$ is divided into two regimes and illustrates linear relations against $(1/T)^{1/3}$. The slope crossover in Figure 2d occurs at ~10 K and could be related to a variance of the hopping distance at T < 10 K. The linear relation strongly indicates a 2D electron hopping process in $Tl_8Sn_{10}Sb_{16}Se_{48}$ that is consistent with the layered structure and weak coupling between the $[Tl_4Sb_6Se_{10}]$ and $[Sn_5Sb_2Se_{14}]$ slabs. Details of the dimension of VRH are discussed in Supporting Information.

Hall coefficient measurements were performed to determine the carrier concentration n and carrier mobility μ. As shown in the inset of Figure 3a, the negative sign of $R_{xy}(H)$ reveals electrons as the dominant charge carriers. The room temperature carrier density is $n_e \approx 8 \times 10^{18}/\text{cm}^3$; n_e decreases with decreasing temperature from 300 to 2 K. The decreasing trend is related to the thermal excitation. A fit to the temperature dependent n_e yields excitation energy gap $\varepsilon_g' \approx 0.12$ eV, which is close to the impurity energy gap value determined by the resistivity analysis. The n_e strongly deviates from the thermal excitation governance below 100 K, and there are no signs of carrier freeze out at low temperature. This phenomenon indicates the existence of additional shallow impurity levels above the major donor level. With a single-band model, the electron mobility μ can be estimated by $\sigma = ne\mu$, where σ denotes conductivity. As shown in Figure 3b, room temperature μ_e is about 6 $\text{cm}^2/(\text{V s})$, and it decreases with falling temperature. The room-temperature μ_e is comparable to bulk MoS_2 at 3 $\text{cm}^2/(\text{V s})$.[5] Above 100 K, μ_e is linearly proportional to $T^{3/2}$ and consistent with impurity scattering theory of heavily doped semiconductors.[13,20] Below 100 K, VRH governs the transport and μ_e saturates and slightly increases as the temperature approaches zero. The cross-plane charge transport of $Tl_8Sn_{10}Sb_{16}Se_{48}$ was a challenge to measure. However, the weak coupling between $[Sn_5Sb_2Se_{14}]$ and $[Tl_4Sb_6Se_{10}]$ layers suggests a substantially poorer conduction than the in-plane value.

The electronic absorption spectrum of the title compound shows a sharp transition between 0.45 and 0.48 eV, yielding a band gap of ~0.45 eV, Figure 3c. The Seebeck coefficient (S) of the polycrystalline sample is −200 μV/K at 300 K and is weakly temperature dependent before the melting temperature of this material, Figure 3d. The negative sign of S points out n-type charge carriers, consistent with the Hall coefficient measurements. The temperature dependent thermal conductivity (κ) of

dx.doi.org/10.1021/ja505301y | J. Am. Chem. Soc. 2014, 136, 11079−11084

the polycrystalline sample is presented in the same figure. The $\kappa \approx 0.45 \pm 0.05$ W/mK at temperatures 300−600 K is significantly smaller than κ = 3.5−1.5 W/mK of the high performance thermoelectric materials PbTe and PbSe−PbS[21,22] and comparable to the reports of the layered semiconductor $(PbSe)(MoSe_2)$.[10] In our polycrystalline samples, the applied thermal flux uniformly diffuses in the misaligned crystals regardless of the anisotropic structure of $Tl_8Sn_{10}Sb_{16}Se_{48}$ and gives rise to an averaged thermal conductivity. For the in-plane direction, the distorted lattice of $[Tl_4Sb_6Se_{10}]$ frustrates the heat diffusion and limits the thermal conduction ability. As to the cross-plane direction, the weak coupling between the slabs $[Sn_5Sb_2Se_{14}]$ and $[Tl_4Sb_6Se_{10}]$ is likely to soften the phonon excitations and retard the thermal transportation. Furthermore, the low κ in superlattice materials[10,23] could provide insight on our observation as well. The interface in the superlattice was proposed to strongly scatter the normal direction heat flow.[24]

For deeper understanding of the electrical transport and optical properties, density functional theory calculations using hybrid functional techniques were performed to study the electronic structure.[25,26] Our calculations show an indirect gap of 0.3 eV from Z to ∼0.4N. The energy band dispersions are presented in Figure 4a. Briefly, the band structure shows substantial anisotropy with in-plane dispersive bands (N-Γ-X in k-space) and off-plane weakly dispersed bands (Z-Γ-L-F-Y in k-space). This anisotropy is rooted in the weak bonding between $[Sn_5Sb_2Se_{14}]$ and $[Tl_4Sb_6Se_{10}]$ layers. Figure 4b is the density of states (DOS) of outer shell electrons for each element. The region shaded red (blue) indicates the total projection onto the $[Sn_5Sb_2Se_{14}]$ ($[Tl_4Sb_6Se_{10}]$) layer of the heterostructure. In the conduction band, near the Fermi energy, the DOS is primarily contributed by Se p orbitals and Sn s orbitals. The DOS of the valence band is made primarily of Se p orbitals and Sb s orbitals. It is worth noting that the electronic orbital levels of the Se and Sb ions in the two different layers do not manifest equally, and the DOS of the CB is primarily localized on the $[Sn_5Sb_2Se_{14}]$ sheet. This can also be seen in Figure 4c, where the majority of conduction electron density is found confined in the $[Sn_5Sb_2Se_{14}]$ sheet. In contrast, the electron density in the $[Tl_4Sb_6Se_{10}]$ slab is small. This disparity of electron density distribution creates a naturally formed heterostructure, which consists of one essentially conducting $[Sn_5Sb_2Se_{14}]$ sheet and one insulating $[Tl_4Sb_6Se_{10}]$ sheet. Our calculations therefore support the 2D origin of electron transport behavior in this material.

The insulating property of the $[Tl_4Sb_6Se_{10}]$ slab likely originates from its lattice distortion. According to the Ioffe−Regel criterion, strong localization of charge carrier leads to an insulating behavior when the electron's mean free path l is smaller than its de Broglie wavelength λ.[27] In the $[Tl_4Sb_6Se_{10}]$ layer, the de Broglie wavelength λ of electrons is estimated as $h/(mv_F) \approx$ 12−1200 Å, where h is Planck constant, m is the half value of bare electron mass for a classical semiconductor, and v_F is Fermi velocity varying 1×10^4 to 1×10^6 m/s for solid state materials.[28] Despite the uncertainty, the estimated λ is greater than the upper limit of electron scattering length of 10 Å, the distortion period in the $[Tl_4Sb_6Se_{10}]$ layer. Therefore, the itinerant electrons are localized in the $[Tl_4Sb_6Se_{10}]$ layer. To lower the total energy, the majority of electron density is confined in the neighboring layer $[Sn_5Sb_2Se_{14}]$, forming a natural heterostructure. Furthermore, the weak coupling between the $[Sn_5Sb_2Se_{14}]$ and $[Tl_4Sb_6Se_{10}]$ layers plays another important role in preventing interlayer coherency. A similar heterostructure has been indicated in layered semiconductor $[PbSe]_5[Bi_2Se_3]_6$,[29] where conductive $[Bi_2Se_3]$ layers hosting nontrivial interface topological insulating states alternate with conduction-poor [PbSe] layers.[30,31]

■ CONCLUSIONS

The new layered narrow-bandgap semiconductor $Tl_8Sn_{10}Sb_{16}Se_{48}$ has alternating and weakly coupled layers of $[Sn_5Sb_2Se_{14}]$ and $[Tl_4Sb_6Se_{10}]$. Conductance measurements demonstrate a 2D characteristic of the electron transport. Hybrid functional calculations unveil a confinement of the majority of electrons in the 2D $[Sn_5Sb_2Se_{14}]$ channels. The distorted $[Tl_4Sb_6Se_{10}]$ layer energetically prohibits electron propagation. This naturally formed heterostructure $[Sn_5Sb_2Se_{14}]$−$[Tl_4Sb_6Se_{10}]$ provides an inspiration in the search for 2D semiconductor band structures using structural module tailoring. $Tl_8Sn_{10}Sb_{16}Se_{48}$ demonstrates low thermal conductivity at room temperature, indicating potential for enhanced thermoelectric performance.

■ EXPERIMENTAL SECTION

Synthesis and crystal growth. High purity Tl(99.9%), Sn(99.99%), Sb_2Se_3(homemade) and Se(99.99%) were weighted in a stoichiometric composition and loaded in a carbon-coated quartz tube. The tube was sealed in vacuum of 10^{-4} mbar and placed inside a second quartz tube and sealed in vacuum of 10^{-4} mbar. The dual-seal can efficiently prevent the escape of Tl element in case of tube breaking. The tubes were heated to 530 °C in 10h, dwelled at that temperature for 10h, then slowly cooled down to 250 °C in 72h followed by natural cooling to room temperature. Black crystals with shining surfaces were selected by mechanically smashing the ingot.

Characterization. Compositions were determined by EDS (Energy Dispersive Spectroscopy) on the Hitachi S-3400N VP-SEM. Single-crystal X-ray diffraction experiments were performed in IPDS 2T diffractometer at room temperature. The structure was solved by direct methods and refined by full-matrix least-squares on F^2 using the SHELXTL program package. Crystals were ground into powder for optical diffuse-reflectance measurements which were carried out at room temperature using a Shimadzu UV-3101 PC double-beam, double monochromator spectrophotometer. The reflectance was converted to absorption to determine the band gap using the Kubelka−Munk function as reported elsewhere.[32,33] Differential thermal analysis (DTA) was performed with a computer-controlled Shimadzu DTA-50 thermal analyzer. The melt grown ingot was carefully polished and cut into a ⌀10 mm × 8 mm cylinder for thermoelectric property measurement. The Seebeck coefficient was measured using an Ulvac Riko ZEM-3 instrument under a low-pressure helium atmosphere from room temperature to ∼550 K. The polycrystalline ingot was cut into a ⌀10 mm × 2 mm disk for the thermal conductivity measurements. The thermal conductivity was calculated from $\kappa = D \cdot C_p \cdot d$, where the thermal diffusivity coefficient (D) was measured using the laser flash diffusivity method in a Netzsch LFA457, the specific heat capacity (C_p) was indirectly derived using a representative sample (Pyroceram 9606) in the range 300−550 K, and the density (d) was determined using the dimensions and mass of the sample. The uncertainty of the Seebeck coefficient and electrical conductivity measurements is 5%. The uncertainty of the thermal conductivity is estimated to be within 8%, considering the uncertainties for D, C_p, and d. The κ of polycrystalline samples is an average of the thermal conductivity of different crystalline directions.

Transport measurements. The monoclinic structure of $Tl_8Sn_{10}Sb_{16}Se_{48}$ can create formidable challenges to cleave crystals into plate shape suitable for the transport measurements. Thin layers were cleaved from bulk crystals both by blade and scotch tape. Electrical contacts were fashioned into Hall-bar geometry. Silver paste was applied on both the surfaces and the edges to ensure reliable electrical contacts. To mitigate any Schottoky barriers, electrical

dx.doi.org/10.1021/ja505301y | J. Am. Chem. Soc. 2014, 136, 11079−11084

contacts were annealed at 250 °C for 1h with the protection of flowing Ar gas. Annealing successfully reduced the contact resistance to less than 200 Ω. Both resistance and Hall coefficient measurements were conducted in the Physical Properties Measurement System (PPMS, Quantum Design). Current of 10 nA was applied along the cleaved surface. Magnetic field is normal to the cleaved surface.

Hybrid functional calculations. Our band structure calculations are based on the Heyd-Scuseria-Ernzerhof (HSE)[25,26] hybrid functional which incorporates a screened admixture of Hartree−Fock type exchange into the standard Perdew−Burke−Ernzerhof (PBE)[34] generalized gradient functional. PBE calculations indicated that inclusion of d-orbital electrons in the valence had negligible effect on the band edges, and hence the hybrid calculations are performed with p-orbital valence and d-electrons within the core. Interactions between ion cores and valence electrons are described by the projector augmented wave method[35,36] as implemented in the VASP code.[37] Plane waves with a kinetic energy cutoff of 200 eV were used as the basis set. Band structure calculations are performed on the primitive cell containing 41 atoms ($Tl_4Sn_5Sb_8Se_{24}$), where the eigenvalues at each *k*-point are determined from a self-consistent calculation of the wave function converged with a 2 × 2 × 2 Monkhorst−Pack[38] sampling of the Brillouin zone.

■ ASSOCIATED CONTENT

Supporting Information

Details of charge transport analysis and X-ray diffraction characterization and single crystal diffraction data in CIF format for $Tl_4Sn_5Sb_8Se_{24}$. This material is available free of charge via the Internet at http://pubs.acs.org.

■ AUTHOR INFORMATION

Corresponding Author

m-kanatzidis@northwestern.edu

Notes

The authors declare no competing financial interest.

■ ACKNOWLEDGMENTS

The transport measurements were supported by the Defense Advanced Research Project Agency (DARPA) (L.F., D.J.W., S.B.Z.) Award No. N66001-12-1-4034. R.G.I. and G.T. were supported by NSF Grant DMR-1104965. Research at Argonne was supported by the US Department of Energy, Office of Science, Office of Basic Energy Sciences, Materials Sciences and Engineering Division (Argonne Contract No. DE-AC02-06CH11357).

■ REFERENCES

(1) Geim, A. K.; Grigorieva, I. V. *Nature* **2013**, *499*, 419−425.
(2) Nicolosi, V.; Chhowalla, M.; Kanatzidis, M. G.; Strano, M. S.; Coleman, J. N. *Science* **2013**, *340*, 1226419.
(3) Bonaccorso, F.; Lombardo, A.; Hasan, T.; Sun, Z.; Colombo, L.; Ferrari, A. C. *Mater. Today* **2012**, *15*, 564−589.
(4) Novoselov, K. S.; Geim, A. K.; Morozov, S. V.; Jiang, D.; Zhang, Y.; Dubonos, S. V.; Grigorieva, I. V.; Firsov, A. A. *Science* **2004**, *306*, 666−669.
(5) Novoselov, K. S.; Jiang, D.; Schedin, F.; Booth, T. J.; Khotkevich, V. V.; Morozov, S. V.; Geim, A. K. *Proc. Natl. Acad. Sci. U. S. A.* **2005**, *102*, 10451−10453.
(6) Radisavljevic, B.; Radenovic, A.; Brivio1, J.; Giacometti, V.; Kis, A. *Nat. Nanotechnol.* **2011**, *6*, 147−150.
(7) Mak, K. F.; Lee, C.-G.; Hone, J.; Shan, J.; Heinz, T. F. *Phys. Rev. Lett.* **2010**, *105*, No. 136805.
(8) Koski, K. J.; Cui, Y. *ACS Nano* **2013**, *7* (5), 3739−3743.
(9) Chiritescu, C.; Cahill, D. G.; Nguyen, N.; Johnson, D. C.; Bodapati, A.; Keblinski, P.; Zschack, P. *Science* **2007**, *315*, 351−353.
(10) (a) Heideman, C. L.; Tepfer, S.; Lin, Q.; Rostek, R.; Zschack, P.; Anderson, M. D.; Anderson, I. M.; Johnson, D. C. *J. Am. Chem. Soc.* **2013**, *135*, 11055−11062. (b) Alemayehu, M. B.; Mitchson, G.; Ditto, J.; Hanken, B.; Asta, M.; Johnson, D. C. *Chem. Mater.* **2014**, *26*, 1859−1866. (c) Beekman, M.; Disch, S.; Rouvimov, S.; Kasinathan, D.; Koepernik, K.; Rosner, H.; Zschack, P.; Neumann, W. S.; Johnson, D. C. *Angew. Chem., Int. Ed.* **2013**, *52*, 13211−13214. (d) Harris, F. R.; Standridge, S.; Johnson, D. C. *J. Am. Chem. Soc.* **2005**, *127*, 7843−7848.
(11) Zhao, L.-D.; Lo, S.-H.; Zhang, Y.; Sun, H.; Tan, G. J.; Uher, C.; Wolverton, C.; Dravid, V. P.; Kanatzidis, M. G. *Nature* **2014**, *508*, 373−377.
(12) Brown, I. D.; Shannon, R. D. *Acta Crystallogr.* **1973**, *A29*, 266−282.
(13) Sze, S. M.; Ng, K. K. *Physics of Semiconductor Devices*; John Wiley & Sons: Hoboken, NJ, 2006.
(14) Shklovskii, B. I., Efros, A. L. *Electron Properties of Doped Semiconductors*; Springer-Verlag: Berlin, 1984.
(15) Mott, N. F. *J. Non-Cryst. Solids* **1968**, *1*, 1−18.
(16) Maji, S.; Mukhopadhyay, S.; Gangopadhyay, R.; De, A. *Phys. Rev. B* **2007**, *75*, No. 073202.
(17) Cabán-Acevedo, M.; Liang, D.; Chew, K. S.; DeGrave, J. P.; Kaiser, N. S.; Jin, S. *ACS Nano* **2013**, *7* (2), 1731−1739.
(18) Tran, P.; Alavi, B.; Gruner, G. *Phys. Rev. Lett.* **2000**, *85*, 1564−1567.
(19) Efros, A. L.; Shklovskii, B. I. *J. Phys. C* **1975**, *8*, L49−L51.
(20) Conwell, E.; Weisskopf, V. F. *Phys. Rev.* **1950**, *77*, 388−390.
(21) (a) He, J. Q.; Zhao, L. D.; Zheng, J. C.; Doak, J. W.; Wu, H. J.; Wang, H. Q.; Lee, Y.; Wolverton, C.; Kanatzidis, M. G.; Dravid, V. P. *J. Am. Chem. Soc.* **2013**, *135*, 4624−4627. (b) Korkosz, R. J.; Chasapis, T. C.; Lo, S. H.; Doak, J. W.; Kim, Y. J.; Wu, C. I.; Hatzikraniotis, E.; Hogan, T. P.; Seidman, D. N.; Wolverton, C.; Dravid, V. P.; Kanatzidis, M. G. *J. Am. Chem. Soc.* **2014**, *136*, 3225−3237. (c) Biswas, K.; He, J. Q.; Blum, I. D.; Wu, C.-I.; Hogan, T. P.; Seidman, D. N.; Dravid, V. P.; Kanatzidis, M. G. *Nature* **2012**, *489*, 414−418.
(22) Androulakis, J.; Todorov, I.; He, J.; Chung, D. Y.; Dravid, V.; Kanatzidis, M. G. *J. Am. Chem. Soc.* **2011**, *133*, 10920−10927.
(23) Venkatasubramanian, R.; Siivola, E.; Colpitts, T.; O'Quinn, B. *Nature* **2001**, *413*, 597−602.
(24) Tamura, S.-I.; Tanaka, Y.; Maris, H. J. *Phys. Rev. B* **1999**, *60*, 2627.
(25) Heyd, J.; Scuseria, G. E.; Ernzerhof, M. *J. Chem. Phys.* **2003**, *118*, 8207−8215.
(26) Krukau, A. V.; Vydrov, O. A.; Izmaylov, A. F.; Scuseria, G. E. *J. Chem. Phys.* **2006**, *125*, No. 224106.
(27) Ioffe, A. F.; Regel, A. R. *Prog. Semicond.* **1960**, *4*, 237.
(28) Ashcroft, N. W.; Mermin, D. N. *Solid State Physics*; Saunders College Publishing: Fort Worth, TX, 1976.
(29) (a) Kanatzidis, M. G. *Acc. Chem. Res.* **2005**, *38*, 359−368. (b) Mrotzek, A.; Kanatzidis, M. G. *Acc. Chem. Res.* **2003**, *36*, 111−119.
(30) Nakayama, K.; Eto, K.; Tanaka, Y.; Sato, T.; Souma, S.; Takahashi, T.; Segawa, K.; Ando, Y. *Phys. Rev. Lett.* **2012**, *109*, No. 236804.
(31) Fang, L.; Stoumpos, C. C.; Jia, Y.; Glatz, A.; Chung, D. Y.; Claus, H.; Welp, U.; Kwok, W.-K.; Kanatzidis, M. *Phys. Rev. B* **2014**, *90*, 020504(R).
(32) Kubelka, P.; Munk, F. *Z. Tekn. Phys.* **1931**, *12*, 593−601.
(33) Hao, S. Q.; Zhao, L. D.; Chen, C. Q.; Dravid, V. P.; Kanatzidis, M. G.; Wolverton, C. M. *J. Am. Chem. Soc.* **2014**, *136*, 1628−1636.
(34) Wang, Y.; Perdew, J. P. *Phys. Rev. B* **1991**, *44*, 13298−13307.
(35) Blochl, P. E. *Phys. Rev. B* **1994**, *50*, 17953−17979.
(36) Kresse, G.; Joubert, D. *Phys. Rev. B* **1999**, *59*, 1758−1775.
(37) Kresse, G.; Hafner, J. *Phys. Rev. B* **1993**, *47*, 558−561.
(38) Monkhorst, H. J.; Pack, J. D. *Phys. Rev. B* **1976**, *13*, 5188−5192.